Effect of carrier mobility on magnetothermoelectric transport properties of graphene

Xinfei Liu,[1] Deqi Wang,[1] Peng Wei,[1] Lijun Zhu,[2] and Jing Shi[1]

[1]*Department of Physics and Astronomy, University of California, Riverside, California 92521, USA*

[2]*Theoretical Division, Center for Nonlinear Studies, Los Alamos National Laboratory, Los Alamos, New Mexico 87545, USA*

(Received 7 February 2012; revised manuscript received 10 June 2012; published 10 October 2012)

With a method to systematically tune the mobility of the same graphene devices, we have investigated the dependence of magnetothermoelectric transport properties of graphene on the carrier mobility. In a zero magnetic field, we find that, as the mobility increases, the Seebeck coefficient S_{xx} exhibits a more pronounced diverging trend near the Dirac point. In an external magnetic field, regular oscillations in S_{xx} are identified corresponding to quantized Landau levels. Only in high-mobility states does an extra pair of peaks and dips in S_{xx} emerge near the Dirac point that persists, at least, to 150 K, and the sign of the peak/dip is reversed as the mobility increases. Based on the signatures in the electrical conductivity and the Hall conductance near the Dirac point, we argue that the extra peak/dip in S_{xx} is associated with an insulating behavior. Furthermore, the main Nernst coefficient peak increases linearly as the mobility increases. Our magnetothermoelectric transport results reflect the contrast in the electronic properties of graphene between low and high carrier mobility states.

DOI: 10.1103/PhysRevB.86.155414 PACS number(s): 68.65.Pq, 73.50.Lw, 65.80.Ck

I. INTRODUCTION

Graphene, a one-atom-thick sheet of carbon atoms densely packed in a honeycomb crystal lattice, has attracted much recent research interest due to its novel electronic, superior thermal, and mechanical properties. Of central interest is its electron-transport property, which is not only determined by its unique band structure, but also strongly influenced by the impurity scattering and interaction effects. For diffusive transport, the carrier mobility of graphene devices is found to be comparable to or larger than that of the conventional semiconductors. For example, a wide range of carrier mobilities, from 1000 to 60 000 $cm^2\,V^{-1}\,s^{-1}$, has been achieved in exfoliated graphene devices on SiO_2 and hexagonal boron nitride substrates.[1,2] Substrate-supported graphene devices are always susceptible to interfacial phonon scattering and scattering from a varying degree of charged impurities in the substrates.[3,4] The absence of those scatterings results in mobility as high as 20 000 $cm^2\,V^{-1}\,s^{-1}$ (Refs. 5 and 6) in suspended devices. In substrate-supported devices, the carrier mobility varies from device to device. By controlling the charged impurity density, a main source of the scattering, the mobility can be modified. It has been shown that, upon introducing metal atoms on top, charge transfer between these adatoms and graphene results in a shift in the Dirac point and, consequently, a degradation in mobility.[7,8] These effects highlight the importance of the disorders, especially, charged impurity scattering, as a disorder effect, in the transport properties of graphene.

Not only disorders affect the electrical transport properties, but also the thermoelectric and magnetothermoelectric transport properties, which are fundamentally connected with the former via the Mott relation. In general, the thermoelectric transport coefficients are related to the energy derivatives of the electrical transport coefficients; therefore, they are more sensitive to changes in the scattering rate. In particular, the sign of the Seebeck coefficient gives the information about the carrier type so that it is sensitive to particle-hole asymmetry. Hence, the thermoelectric transport serves as a unique tool to probe various effects on diffusive transport in graphene. The disorder effect on magnetothermoelectric transport has been studied in both theories[9–11] and experiments.[12–16] For example, the dependence of S_{xx} and S_{xy} on carrier mobility was theoretically predicted for various regimes of classical transport.[17] In Landau quantizing magnetic fields, a universal scaling for both electrical and thermoelectric transport coefficients was found for various disorder strengths.[11] Although the experimental results for high Landau levels (LLs) are in agreement with theories, there is a discrepancy in the polarity (the sign) of the Seebeck coefficient near the zeroth LL.[11] In most experiments, graphene devices have random and fixed mobility values so that the direct relationship between the transport coefficients and the mobility could not be easily established experimentally. Recently, we have shown that the low-temperature mobility of graphene can be reversibly tuned via controlling the high-temperature resistance level using ligand-bound Fe_3O_4 nanoparticles plus toluene molecules.[18] In the same device, different resistance levels at room temperature represent different charge states of the graphene sheet. The room-temperature charge neutral state or the highest resistance state gives rise to the highest mobility state at low temperatures; a low room-temperature resistance state, on the other hand, gives rise to a relatively low mobility at low temperatures. This reversible tunability offers an unprecedented opportunity to systematically study the charge impurity effect on transport properties in the same graphene devices. It is the objective of this paper to establish the dependence of the magnetothermoelectric transport properties of single-layer graphene on the carrier mobility with this new capability.

II. EXPERIMENTAL DETAILS

Exfoliated single-layer graphene devices are fabricated on SiO_2/Si using standard electron-beam lithography as described elsewhere.[13,15] As shown in the inset of Fig. 1(b), several pairs of Cr(10-nm)/Au(80-nm) leads are deposited for generating heat (left side of the sample) and measuring both longitudinal and transverse thermovoltage responses ΔV_x (1 and 6) and ΔV_y (2 and 4 and 3 and 5), local temperatures (1

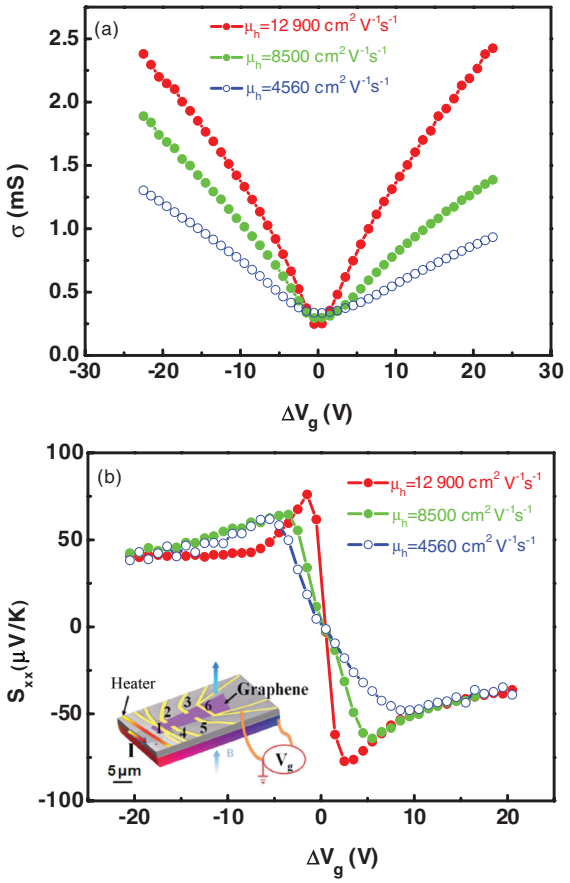

FIG. 1. (Color online) (a) Zero-field electrical conductivity σ and (b) Seebeck coefficient S_{xx} vs ΔV_g of device A measured at 150 K with three mobility values. ΔV_g is the gate voltage relative to the Dirac point. The inset of (b) is a false-colored scanning electron microscopy image of a graphene device. The graphene flake is connected to multiple leads for different purposes: 1 and 6 are for both thermovoltages and local thermometry via four-terminal resistivity; 2 and 4 and 3 and 5 are for Hall and Nernst voltages. A heater is located on the left end.

and 6) and, therefore, the temperature difference ΔT along the longitudinal direction in response to heating. The local temperatures are measured by the resistance thermometry, which consists of two short segments of Cr/Au spanning across the graphene flake, whose four-terminal resistance is recorded before and after the heater is turned on. The resistance change in these thermometers is converted to the local temperature change by comparing with the premeasured resistance vs temperature curve for Cr/Au segments. This resistance thermometry allows us to measure small temperature rises for temperatures below room temperature and down to ~10 K. Typically, we adjust the heater power to generate a temperature difference of ~80–300 mK between the two inner voltage leads that are spaced ~5–10 μm apart, which is large enough to generate measurable thermo-emf signals but small enough to stay in the linear-response regime. At each temperature, both the thermovoltage responses and the temperature changes between heater on and heater off are obtained. With these measurements, the Seebeck and Nernst coefficients are determined by $S_{xx} = -\frac{\Delta V_x}{\Delta T}$ and $S_{xy} = -S_{yx} = \frac{\Delta V_y}{\Delta T}\frac{L}{W}$, respectively, with L being the separation between the thermometry contacts and W being the separation of the transverse voltage contacts. A description of the thermoelectric measurement method on graphene devices has also been reported previously.[13] We have carried out low-temperature magnetotransport and magnetothermoelectric transport measurements in either an Oxford He3 or a Physical Property Measurement System (PPMS), which covers the temperature range of 2–300 K and a magnetic field up to 8 T (He3) or 14 T (PPMS), respectively. The electrical resistivity is measured using the four-terminal method with an ac current source and a lock-in amplifier. The current amplitude for electrical measurements is below 0.1 μA.

Results from two graphene devices (A and B) are reported in this paper. Device A has three distinct mobility states, and device B has four distinct mobility states. The mobility tuning is accomplished by the procedures described in Ref. 18. In the presence of a charge reservoir provided by a fully dried toluene solution containing ligand-bound Fe_3O_4 nanoparticles, graphene tends to slowly give away, to the reservoir, the charges (electrons or holes) loaded with a gate voltage, causing the graphene resistance to increase over time. Eventually, graphene approaches its charge neutral point after a period of ~1 to 2 h at room temperature. If the charge neutral state or the maximum resistance is reached and the device is cooled down to low temperatures, the highest mobility state is obtained. The resistance maximum state can be achieved with any gate voltage, provided that the device is held at the gate voltage for a sufficiently long time after the gate voltage is turned on. Depending on the charge state indicated by its resistance prior to cooling, the resulting low-temperature mobility varies accordingly. By controlling the room-temperature resistance level, a range of low-temperature mobilities can be set in the same devices. In the meantime, the charge neutral point in the low-temperature gate voltage sweeps can vary depending on the initial condition, such as the amount of waiting time and the gate voltage as discussed in Ref. 18. Below 250 K, once a mobility value is set, it stays unchanged for a fixed temperature. Magnetothermoelectric measurements are performed in each mobility state set in this way.

III. EFFECT OF MOBILITY ON ZERO-FIELD ELECTRICAL AND THERMOELECTRIC TRANSPORTS

We first study the transport properties in a zero magnetic field. Figure 1(a) shows the electrical conductivity σ vs relative gate voltage ΔV_g for three different mobility states in device A, and Fig. 1(b) shows the corresponding Seebeck coefficient S_{xx} of the same device at those mobility states, measured in a zero magnetic field at 150 K. Since there is a variation in the position of the Dirac point (or the charge neutrality point) among the three mobility states, here, we plot these data relative to the Dirac point, i.e., using the relative gate voltage ΔV_g with reference to the Dirac point. For the three mobility states we obtained, the Dirac point is located at 16.5, 1.5, and 1.5 V in V_g. In Ref. 18, we found that the Dirac point and the mobility can be tuned independently. Therefore, here, we do not attempt to extract any information from the absolute position of the Dirac point for different mobility states.

To calculate the carrier mobility for device A, we first find the carrier density for a given relative gate voltage using $C_g = 115$ aF/μm^2, the capacitance of the graphene/SiO_2/Si capacitor with a 300-nm-thick SiO_2. The slope of the conductivity vs charge density near the Dirac point is the mobility value we refer to in this paper. In the pristine state, the mobility is approximately 4560 cm^2 V^{-1} s^{-1} at 150 K. After adding a nanoparticle-containing toluene solution (six drops) and cooling with an intermediate room-temperature resistance, the mobility is increased to 8500 cm^2 V^{-1} s^{-1}. By cooling the device with a higher room-temperature resistance, i.e., closer to the Dirac point, its mobility is further increased to 12 900 cm^2 V^{-1} s^{-1}. With similar procedures, the mobility of device B can be tuned into four different states: 7000, 9330, 15 330, and 17 000 cm^2 V^{-1} s^{-1}. In Fig. 1(b), the Seebeck coefficient passes zero at the Dirac point where the carrier type switches. For holes (left of the Dirac point), S_{xx} is positive; for electrons, it is negative. As the carrier density approaches zero, the magnitude of S_{xx} first increases, then reaches a maximum, and decreases toward zero. This general gate-tunable feature in S_{xx} is true even for bilayer graphene devices.[19–21] For different mobility states, the maximum value of S_{xx} varies. It increases from ~50 to 75 μV/K as the mobility varies from 4560 to 12 900 cm^2 V^{-1} s^{-1}. Another salient feature is the more divergent trend in S_{xx} observed in high-mobility states, accompanied by a sharper peak-to-dip transition around the Dirac point.

Clearly, the low-mobility state has a broader minimum conductivity plateau [Fig. 1(a)], which is consistent with earlier experimental observations.[1,15] From Fig. 1(b), the low-mobility state also has a broader peak-to-dip transition in S_{xx}. The width of the minimum conductivity plateau has been previously shown to be associated with the concentration of charged impurities in graphene.[1] We conclude that the peak-to-dip width in S_{xx} is also related to this disorder effect. In low-mobility states, the divergent trend is significantly smeared. The diverging behavior was previously found to vary with the effective carrier density n in the vicinity of the Dirac point as $\sim\frac{1}{\sqrt{n}}$.[13] Note that S_{xx} for all mobility states converges to the same values at high gate voltages on both electron and hole sides. At high ΔV_g, we expect that the effective carrier density n is much greater than the charge density fluctuations n^* induced by charged impurities near the Dirac point. Therefore, for different carrier mobility states, as n^* varies, S_{xx} differs significantly only near the Dirac point and becomes more divergent when n^* decreases. We conclude that the more divergent behavior in higher-mobility states is a consequence of smaller n^* due to the reduced concentration of charged impurities.

IV. EFFECT OF MOBILITY ON MAGNETOTHERMOELECTRIC TRANSPORT: 150-K DATA

When a magnetic field is applied in addition to the longitudinal voltage response (Seebeck effect), a transverse thermoelectric voltage response (Nernst signal) also starts to develop in the presence of a temperature gradient. Figures 2(a) and 2(b) show a direct comparison of S_{xx} between two mobility states: 8500 and 12 900 cm^2 V^{-1} s^{-1} of sample A for a set of magnetic fields measured at 150 K. At and below 2 T, S_{xx}

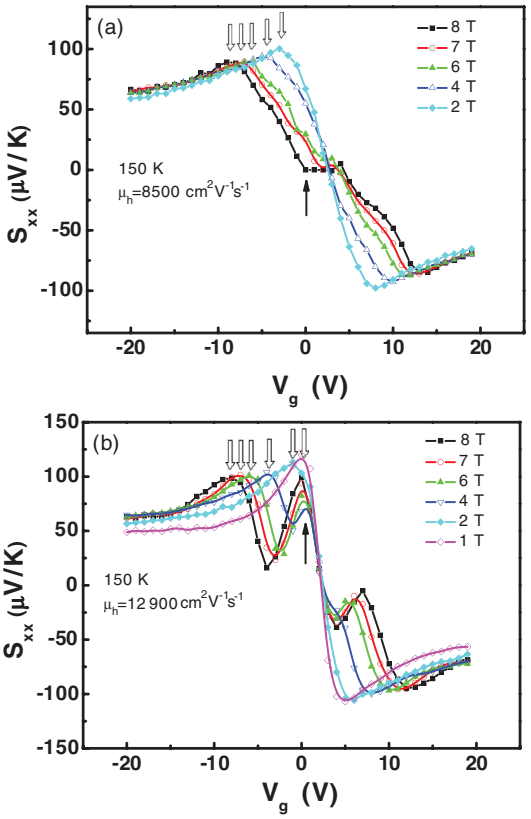

FIG. 2. (Color online) Seebeck coefficient S_{xx} vs V_g for different magnetic fields in (a) low-mobility and (b) high-mobility states of device A measured at 150 K. Open arrows in both (a) and (b) indicate the position of the main peak at different magnetic fields. The solid arrow in (b) indicates the new peak near the Dirac point at high magnetic fields.

has a similar behavior as the zero-field data [Fig. 1(b)] except that the peak and dip positions (arrows) shift to larger V_g. At higher magnetic fields, in the low-mobility state, the main peaks and dips continue extending to higher V_g, leaving a broader peak-to-dip transition near the Dirac point. At 8 T, a small plateau region at the Dirac point becomes visible. In astounding contrast, in the high-mobility state of the same device [Fig. 2(b)], an additional pair of sharp peaks and dips appears near the Dirac point starting from 4 T, whereas, the main peaks and dips are pushed to higher V_g as in the low-mobility state. These subfeatures close to the Dirac point grow in magnitude and shift their positions to higher V_g as the magnetic-field strength increases. Compared with the low-mobility state, the main peak/dip features correspond to each other in magnitude and position. It is the additional subfeatures that distinguish the two mobility states. The plateau in the low-mobility state in the vicinity of the Dirac point at 8 T could be just a precursor of the fully developed subfeatures observed in the high-mobility state starting to appear even at low magnetic fields. This is in sharp contrast with the behavior of S_{xx} reported earlier, which was measured on graphene samples with mobilities less than 5000 cm^2 V^{-1} s^{-1}.[12,13] In those low-mobility samples, S_{xx} also has an extra peak and dip, but all with an opposite polarity, i.e., being negative (positive) on the hole (electron) side, which has an opposite sign with

respect to that of the LL peaks (dips). In comparison, for the high-mobility sample in Fig. 2(a), however, the signs of the subfeatures are the same as the respective S_{xx} peaks/dips at high LLs, i.e., the regular polarity.

From $\boldsymbol{J} = \sigma \boldsymbol{E} + \alpha(-\nabla T)$, where $\boldsymbol{J}$ is the electric current and $\boldsymbol{E}$ is the electric field, both thermoelectric coefficients S_{xx} and S_{xy} are related to the tensor elements of the conductivity σ (or resistivity ρ) and the thermoelectric conductivity α. For the Seebeck coefficient S_{xx}, $S_{xx} = \rho_{xx}\alpha_{xx} - \rho_{xy}\alpha_{xy}$, where ρ_{xy} and α_{xy} are the Hall resistivity and transverse thermoelectric conductivity and ρ_{xx} and α_{xx} are the longitudinal counterparts. At higher LLs, S_{xx} has a definitive sign for electrons or holes as it is dominated by the contribution from the second term $\rho_{xy}\alpha_{xy}$. However, as both ρ_{xy} and α_{xx} change signs at the zeroth LL, S_{xx} changes sign as well, but its polarity is determined by the relative strength of the two terms $\rho_{xx}\alpha_{xx}$ and $\rho_{xy}\alpha_{xy}$. In the theoretical paper based on a noninteracting model, the opposite polarity is found to be a disorder effect,[11] i.e., depending on whether the disorder-broadened LL width is much larger or smaller than the scale of $k_B T$, the polarity can be opposite or regular, respectively. Our experiments present an observation that the polarity of S_{xx} switches when the mobility increases at a fixed temperature, which seems to be in agreement with this prediction. However, as we discuss later, the regular polarity observed in our high-mobility state is due to another possibility, i.e., the zeroth LL splits into two distinct electron and hole LLs.

Figure 3(a) shows the Nernst signal S_{xy} at 150 K in device A with three different mobility states. S_{xy} has a main peak at the Dirac point, accompanied by a pair of side dips and peaks as observed previously.[12–14] In different mobility states, the central peak position (or the Dirac point) varies slightly. We also plot the data with reference to the Dirac point using ΔV_g. In the highest mobility ($12\,900\ \mathrm{cm^2\ V^{-1}\ s^{-1}}$) state, the Nernst peak height $(S_{xy})_{\max}$ per unit magnetic field reaches $\sim 22\ \mu\mathrm{V\ K^{-1}\ T^{-1}}$, which is over four times larger than the previously reported value $\sim 5\ \mu\mathrm{V\ K^{-1}\ T^{-1}}$).[13] As the mobility increases, $(S_{xy})_{\max}$ increases, and the full width at half maximum (FWHM) decreases. As shown in the inset of Fig. 3(a), $(S_{xy})_{\max}$ is directly proportional to the carrier mobility. It is usually impractical to compare S_{xy} among different samples with different native mobility values. The samples with tunable mobility allow us to compare the effect of disorder and to draw reliable conclusions about the carrier mobility dependence. For a fixed mobility state, we also measure the Nernst peak at different magnetic fields. In the highest mobility ($12\,900\ \mathrm{cm^2\ V^{-1}\ s^{-1}}$) state, the magnetic-field dependence of S_{xy} is displayed in Fig. 3(b). At low fields (<2 T), no side features are present near the central peak. As the magnetic-field strength increases, two side dips appear with a slight asymmetry, accompanying the linear increase in the central peak height. It is interesting to note that, in the high-mobility state, the FWHM of the central peak is broadened by the magnetic-field strength. Figure 3(a) shows the effect of the mobility on the FWHM of the central peak. As the mobility decreases, the central peak is clearly broadened. By comparing S_{xx} with S_{xy} in Figs. 2(b) and 3(b), we do not observe any obvious features in S_{xy} that correspond to the subfeatures in S_{xx}.

To resolve the subfeatures in S_{xx} that emerge in high-mobility states, we have carried out more detailed measurements of S_{xx} up to 14 T on another high-mobility sample at 150 K (device B, with the highest mobility of $17\,000\ \mathrm{cm^2\ V^{-1}\ s^{-1}}$). Similar to device A, the subfeatures near the Dirac point are clearly observed [Fig. 4(a)]. There is an asymmetry between the electron and the hole sides. The main peaks and dips at $V_g \sim \pm 20$ V correspond to those in device A. Compared with the low-temperature results in σ_{xy}, these main peaks/dips can be identified as the first LLs, i.e., $n = -1$ and $n = 1$, respectively, labeled H1 and E1 accordingly in the inset. Thus, the subfeatures likely originate from the split zeroth LL, labeled H0 and E0 in the inset. The former is, for the peak (positive in S_{xx}), characteristic of hole states, and the latter is, for the dip (negative in S_{xx}), characteristic of electron states. By tracking the magnetic-field dependence of the subfeature positions in V_g of E0, H0, E1, and H1, we find that the positions in V_g change linearly with the magnetic-field strength [Fig. 4(b)]. The top and bottom lines are for $n = \pm 1$ LLs, respectively, and the two inner lines are for the two subfeatures. The linear magnetic-field dependence indicates that the degeneracy of the LLs is proportional to the magnetic field. The slope of the H1 and E1 lines is approximately four times as large as that of H0 and E0 in this device at 150 K. As shown in the inset, corresponding well to the subfeatures in S_{xx} at 8 T, there are two peaks in σ_{xx} that are located between the $+1$ and the -1 features; therefore, these peaks are identified with the zeroth LL. A

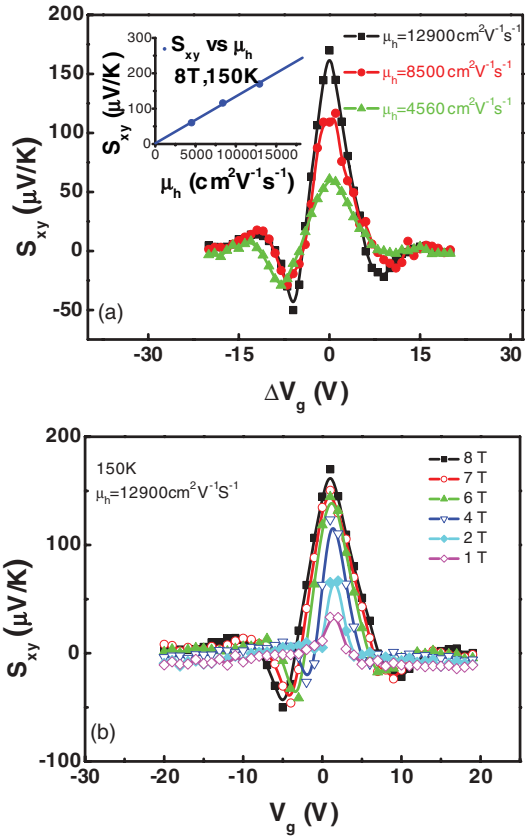

FIG. 3. (Color online) (a) Nernst signal S_{xy} at 8 T vs ΔV_g for different mobility states of sample A at 150 K. The inset shows the linear dependence of the central Nernst peak height on carrier mobility. (b) Magnetic-field dependence of S_{xy} of the same device in the highest-mobility state.

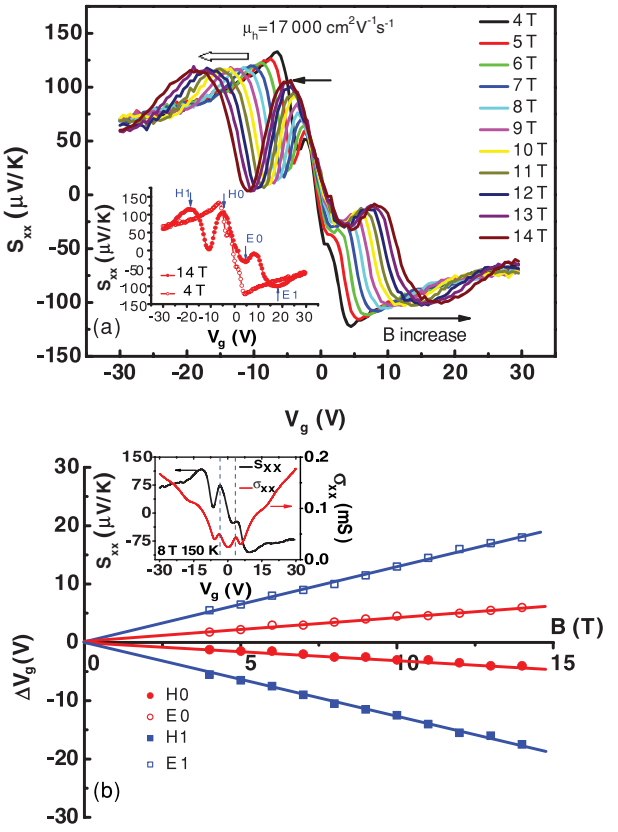

FIG. 4. (Color online) (a) Seebeck coefficient S_{xx} of device B at its highest-mobility state measured at 150 K up to 14 T. The open arrow shows the major peak shift as a function of the magnetic field, and the solid arrow shows the shift in the new peak near the Dirac point. The inset shows the contrast between two magnetic fields (4 and 14 T). (b) The magnetic-field dependence of the peak positions associated with E0, H0, E1, and H1 as labeled in the inset of (a). The inset of (b) shows the double-peak feature in σ_{xx} measured at 150 K that corresponds to the subfeatures in S_{xx} measured at the same temperature. In both σ_{xx} and S_{xx}, the corresponding first-LL features are also shown at higher gate voltages.

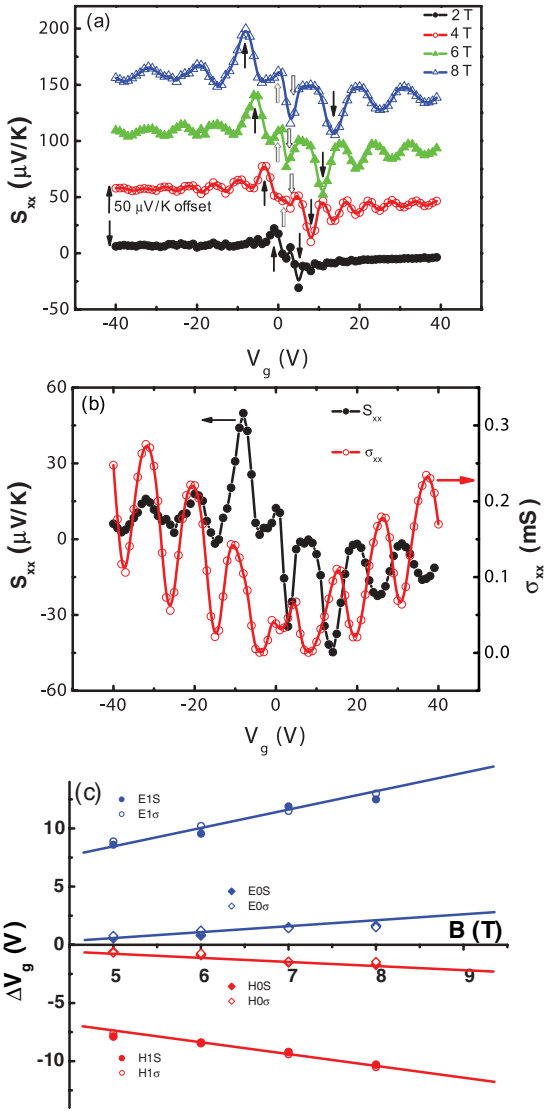

FIG. 5. (Color online) (a) Quantum oscillations in S_{xx} vs V_g for different quantizing magnetic fields for device A at 20 K (curves are offset for clarity). Open and solid arrows indicate the first- and zeroth-LL features as well as their position shifts as the magnetic field is varied. (b) Both σ_{xx} and S_{xx} taken at 20 K are plotted together to show the correspondence of the subfeatures near the Dirac point. (c) Positions of E0, H0, E1, and H1 identified from σ_{xx} and S_{xx} (labeled by E0σ, E0S, etc.) measured at 20 K vs the magnetic field.

similar double-peak feature was previously found in 14 T up to 100 K.[22] In the high-mobility state of our samples, the zeroth LL feature persists to 150 K at 8 T, indicating a larger energy splitting. A more systematic temperature dependence study is needed to identify the physical origin of the zeroth LL splitting for graphene devices with tunable mobility.

V. EFFECT OF MOBILITY ON LOW-TEMPERATURE MAGNETOTHERMOELECTRIC TRANSPORT

We further examine the low-temperature magnetothermoelectric data. At 20 K, both S_{xx} and S_{xy} develop a series of quantum oscillations in the high-mobility state of device A as shown in Figs. 5(a) and 6(a) for selected quantizing magnetic fields. The evenly spaced peaks and dips in S_{xx} are identified as LLs, i.e., $n = \pm 1, \pm 2, \pm 3, \ldots$, in S_{xx}, as they are matched well with the characteristic half-integer quantum Hall features in σ_{xx} in Fig. 5(b) and the plateaus in σ_{xy} (not shown) taken under the same conditions. As shown in Fig. 5(a), the occurrence and evolution of the subfeatures (open arrows) in S_{xx} as a function of the applied magnetic field are evident. The subfeatures continue to have the same polarity as that of the high LL peaks and dips, consistent with the observations at 150 K. At low fields, both the magnitude and the period of the quantum oscillations are smaller. Compared with the low-mobility states, the high-mobility states show more oscillations for the same gate voltage range. At 4 T, as many as six LLs can be clearly identified on each side.

At 20 K, similar to S_{xx}, more side peaks associated with more LLs are seen in S_{xy}. In fact, the peaks and dips in S_{xx} correspond well to the zeros in S_{xy}, which are consistent with earlier observations.[13] In the highest-mobility state of device A, $(S_{xy})_{\max}$ is also proportional to the magnetic

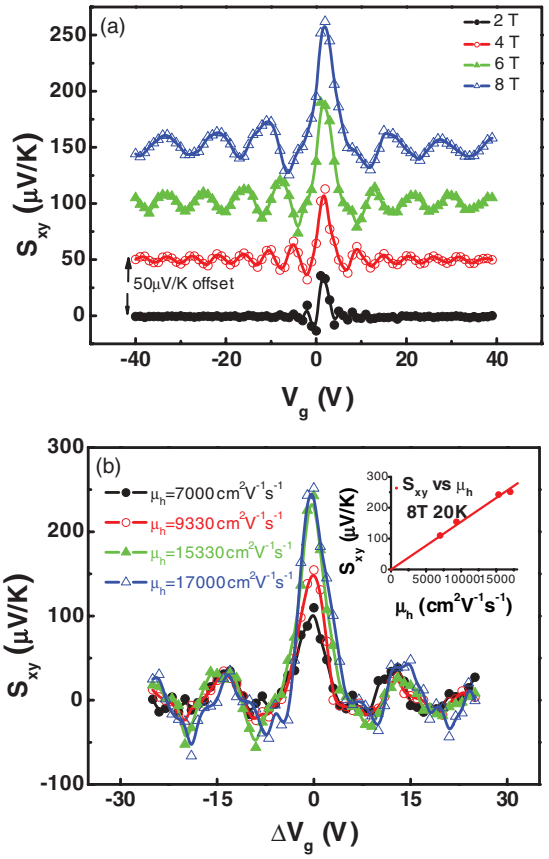

FIG. 6. (Color online) (a) Quantum oscillations in S_{xy} for different quantizing magnetic fields for device A at 20 K. (b) S_{xy} for device B measured at 8 T and 20 K for four different mobility states. The inset shows the linear dependence of the central S_{xy} peak height on carrier mobility.

field with a slope $\sim 19\,\mu\mathrm{V\,K^{-1}\,T^{-1}}$, comparable with that at 150 K. In device B, the low-temperature peak height $(S_{xy})_{\max}$ also increases as the mobility increases [Fig. 6(b)], whereas, the other side peaks do not seem to be sensitive to the mobility change. Similar linear mobility dependence of $(S_{xy})_{\max}$ is observed as shown in the inset of Fig. 6(b). This mobility dependence agrees qualitatively with the theoretical calculations with different degrees of disorder.[11] Hence, the Nernst effect may serve as a unique probe for studying the effect of disorder in graphene.

As shown in Fig. 5(b), we also observe a double-peak feature in σ_{xx}, which corresponds well to the subfeatures in S_{xx}. The double-peak feature persists to $\sim$150 K as previously shown in the inset of Fig. 4(b). In measured ρ_{xx} vs V_g, the zeroth LL is characterized by the highest central peak, and no subfeatures can be seen near the Dirac point. The pronounced double-peak feature is only resolved in σ_{xx} after the inverse of the resistivity tensor is calculated. However, in S_{xx}, not only the subfeatures are visible in raw data, but also the polarity information is contained. In Fig. 5(c), the magnetic-field dependence of the double peaks in σ_{xx} and the corresponding subfeatures in S_{xx} are plotted along with the positions of the first LL peaks.[23] Clearly, the position of all features follows linear magnetic-field dependence. The double-peak feature in σ_{xx} near the Dirac point reveals a diminished conductivity at the zeroth LL, which, in turn, implies an insulating state emerging in high magnetic fields probably as a result of the splitting of the zeroth LL. As this feature only exists in high-mobility samples, we could rule out the disorder-driven quantum Hall liquid-to-insulator transition. The physical origin of the insulating state has been the subject of extensive discussions.[22,24–27] Although the subfeatures in S_{xx} alone can be just an intrinsic effect of the zeroth LL as indicated by the numerical calculations based on noninteracting electrons with disorder,[11] the correlation with the double-peak structure in σ_{xx} suggests an insulating state arising from the splitting of the zeroth LL in high-mobility graphene. Another indication is from the peak value of S_{xy}, which is determined dominantly by α_{xy}/σ_{xx} because $\sigma_{xx} \approx 0$. As α_{xy} saturates to a universal value at high temperatures while σ_{xx} reduces at the Dirac point with the emergence of an insulating state, $(S_{xy})_{\max}$ is greatly enhanced. The linear dependence of $(S_{xy})_{\max}$ on mobility also suggests that the minimum conductivity in the insulating state is inversely proportional to the carrier mobility. Hence, a thorough study of both electrical and thermoelectric transport properties in high-mobility graphene may shed light on the fundamental origin of the subfeatures and related zeroth LL splitting. We note that the absence of subfeatures in S_{xy} in a gapped system is also observed in gapped bilayer graphene due to a bias voltage between two layers.[21]

VI. CONCLUSION

To summarize, we have investigated the thermoelectric transport properties in the same devices with systematically tuned carrier mobility. In high-mobility samples, thermoelectric transport coefficients reveal additional features even at relatively high temperatures and modest magnetic fields. The polarity of the subfeatures is associated with the degree of disorder as predicted. In high-mobility states, the polarity of the subfeatures sides with that of the main LL features. Similar to high LL peak positions, the subfeature positions follow the same linear magnetic-field dependence. Those additional features are found to be correlated with the double-peak feature in the conductivity, suggesting an insulating state due to the splitting of the zeroth LL. In addition, we have demonstrated that the central Nernst peak at the Dirac point is directly proportional to the carrier mobility. The sensitivity of the thermoelectric transport coefficients to the detailed electronic structure near the Dirac point offers a new possibility to explore the origin of the zeroth LL splitting in graphene.

ACKNOWLEDGMENTS

We wish to thank L. Pryadko and D. N. Sheng for useful discussions. The research was sponsored, in part, by DARPA/Defense Microelectronics Activity (DMEA) under Agreement No. H94003-10-2-1004 (X.L. and D.W.), by the US Department of Energy, Office of Basic Energy Sciences, Division of Materials Sciences and Engineering under Award No. DE-FG02-07ER46351 (P.W. and J.S.), and the US DOE through the LDRD program at LANL (L.Z.).

[1]Y.-W. Tan, Y. Zhang, K. Bolotin, Y. Zhao, S. Adam, E. H. Hwang, S. Das Sarma, H. L. Stormer, and P. Kim, Phys. Rev. Lett. **99**, 246803 (2007).
[2]C. R. Dean *et al*., Nat. Nanotechnol. **5**, 722 (2010).
[3]J. H. Chen, C. Jang, S. Xiao, M. Ishigami, and M. S. Fuhrer, Nat. Nanotechnol. **3**, 206 (2008).
[4]S. Adam *et al*., Proc. Natl. Acad. Sci. USA **104**, 18392 (2007).
[5]X. Du, I. Skachko, A. Barker, and E. Y. Andrei, Nat. Nanotechnol. **3**, 491 (2008).
[6]K. I. Bolotin, K. J. Sikes, J. Hone, H. L. Stormer, and P. Kim, Phys. Rev. Lett. **101**, 096802 (2008).
[7]J. H. Chen *et al*., Nat. Phys. **4**, 377 (2008).
[8]K. M. McCreary, K. Pi, A. G. Swartz, W. Han, W. Bao, C. N. Lau, F. Guinea, M. I. Katsnelson, and R. K. Kawakami, Phys. Rev. B **81**, 115453 (2010).
[9]V. Ugarte, V. Aji, and C. M. Varma, Phys. Rev. B **84**, 165429 (2011).
[10]V. P. Gusynin and S. G. Sharapov, Phys. Rev. B **73**, 245411 (2006).
[11]L. Zhu, R. Ma, L. Sheng, M. Liu, and D. N. Sheng, Phys. Rev. Lett. **104**, 076804 (2010).
[12]Y. M. Zuev, W. Chang, and P. Kim, Phys. Rev. Lett. **102**, 096807 (2009).
[13]P. Wei, W. Z. Bao, Y. Pu, C. N. Lau, and J. Shi, Phys. Rev. Lett. **102**, 166808 (2009).
[14]J. G. Checkelsky and N. P. Ong, Phys. Rev. B **80**, 081413 (2009).
[15]D. Wang and J. Shi, Phys. Rev. B **83**, 113403 (2011).
[16]X. Liu, Z. Ma, and J. Shi, Solid State Commun. **152**, 469 (2012).
[17]V. P. Gusynin and S. G. Sharapov, Phys. Rev. B **73**, 245411 (2006).
[18]D. Wang, X. Liu, L. He, Y. Yin, D. Wu, and J. Shi, Nano Lett. **10**, 4989 (2010).
[19]L. Hao and T. K. Lee, Phys. Rev. B **81**, 165445 (2010).
[20]S.-G. Nam, D.-K. Ki, and H.-J. Lee, Phys. Rev. B **82**, 245416 (2010).
[21]C.-R. Wang, W.-S. Lu, and W.-L. Lee, Phys. Rev. B **82**, 121406(R) (2010).
[22]J. G. Checkelsky, L. Li, and N. P. Ong, Phys. Rev. Lett. **100**, 206801 (2008).
[23]In sample A, there is a systematic mismatch between the resistivity peaks and the corresponding conductivity peaks at all LLs. However, there is a perfect match between the Seebeck peaks and the resistivity peaks at all LLs. Both resistivity and Seebeck peaks are raw experimentally measured data up to a constant; therefore, the peak positions remain unchanged after the absolute values are computed. However, after the inverse tensor calculation, we find that the conductivity peak positions are shifted slightly. A possible reason for this shift is that the real aspect ratio of the sample may be different from the apparent aspect ratio defined by the Hall bar geometry. This difference could be caused by a nonuniform nanoparticle distribution on graphene for low-density particle samples, which created relatively high conductivity paths in graphene. Consequently, the actual aspect ratio is larger. By adjusting the aspect ratio, we have aligned all LL peaks between ρ_{xx} and σ_{xx}. Then, the double peaks in σ_{xx} are aligned with the subfeatures in S_{xx}, and their peak positions are read to generate Fig. 5(c).
[24]D. A. Abanin, P. A. Lee, and L. S. Levitov, Phys. Rev. Lett. **96**, 176803 (2006).
[25]D. A. Abanin, K. S. Novoselov, U. Zeitler, P. A. Lee, A. K. Geim, and L. S. Levitov, Phys. Rev. Lett. **98**, 196806 (2007).
[26]Y. Zhang, Z. Jiang, J. P. Small, M. S. Purewal, Y.-W. Tan, M. Fazlollahi, J. D. Chudow, J. A. Jaszczak, H. L. Stormer, and P. Kim, Phys. Rev. Lett. **96**, 136806 (2006).
[27]Z. Jiang, Y. Zhang, H. L. Stormer, and P. Kim, Phys. Rev. Lett. **99**, 106802 (2007).